Journal of Energy Storage 128 (2025) 117023

Contents lists available at ScienceDirect

Journal of Energy Storage

journal homepage: www.elsevier.com/locate/est

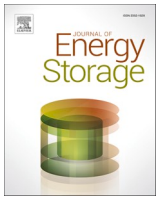

Research papers

# 0D electrochemical modelling of sulfur cathodes

Hamid Mollania [a], Majid Oloomi-Buygi [a,*], Andreu Cabot [b,c,*]

[a] Ferdowsi University of Mashhad, Department of Electrical Engineering, Mashhad 9177948974, Iran
[b] Catalonia Institute for Energy Research - IREC, Sant Adrià de Besòs, Barcelona 08930, Spain
[c] ICREA, Pg. Lluís Companys 23, 08010 Barcelona, Catalonia, Spain.

ARTICLE INFO

*Keywords:*
Bayesian optimization
lithium–sulfur battery
Sulfur cathode
Polysulfide
Electrochemical model

ABSTRACT

Sulfur cathodes represent a promising solution to meet the growing demand for cost-effective, sustainable, and high-energy-density energy storage systems utilizing abundant elements. However, their commercialization remains challenging due to the complex metal-sulfur reactions, which often involve solid-liquid phase transitions, as well as the dissolution and migration of polysulfides. Addressing these challenges requires a deeper understanding and systematic optimization of these processes. In this study, we present a three-step zero-dimensional (0D) electrochemical model based on Nernst formulations and Butler–Volmer kinetics designed to simulate the performance of sulfur cathodes. Focusing on lithium-sulfur batteries (LSBs) as a case study, the model incorporates key phenomena, including the multiple electrochemical reactions involved in the conversion of sulfur to lithium sulfide, precipitation of $S^{2-}$, and the shuttle effect. To validate the model, we utilize sulfur cathodes composed of $Li_2S$ supported on Ketjen Black (KB) and incorporating cobalt nanoparticles ($Li_2S$-Co@KB). The developed model is employed to simulate discharge curve using a hybrid optimization approach combining Bayesian and the Nelder-Mead algorithms. The model's predictive capability is evaluated by assessing its ability to replicate the experimental voltage profiles of LSBs. Additionally, the error between the simulated and experimental voltage curves is analyzed to demonstrate the model's accuracy and reliability.

## 1. Introduction

Sulfur cathodes have attracted significant interest due to their high theoretical energy density, reliance on abundant resources, and potential for cost-effectiveness and sustainability [1–3]. However, the optimization of LSBs for commercial use has been hindered by the complexity of sulfur redox reactions, involving multiple steps, the formation of often soluble polysulfides, the slow nucleation of solid species, and the inherent low electrical conductivity of sulfur and lithium sulfide [4–6].

Current research focuses on mitigating the polysulfide loss and enhancing sulfur utilization. This is achieved by employing porous sulfur host materials with high electrical conductivity, polar sites for polysulfide binding, and porous structures capable of accommodating volumetric changes while facilitating efficient ionic and electronic transport [7–11]. Despite extensive efforts, the complexity of the system has led to predominantly trial-and-error engineering approaches, hindering progress toward knowledge-driven design. Advancing the field requires a more rational approach, supported by the development of accurate models capable of simulating the intricate electrochemical behaviour of LSBs and extracting critical parameters at the cell level.

The sulfur redox processes in LSBs involve several electrochemical steps that translate into a nonlinear differential algebraic structure. The galvanostatic charge-discharge profiles are generally characterized by two discharge and charge plateaus (Fig. 1). The high voltage discharge plateau, at 2.3–2.4 V corresponds to the initial reduction of elemental sulfur ($S_8$) to soluble higher-order lithium polysulfides ($Li_2S_x$, where x = 4–8). This phase involves the dissolution of sulfur and the formation of long-chain polysulfides in the electrolyte. The low voltage discharge plateau, at 2.0–2.1 V, is associated with the further reduction of the higher-order polysulfides to shorter chain polysulfides and eventually to insoluble lithium sulfide ($Li_2S$), involving a solid-phase deposition step. During charging, two plateaus, though closer in potential, 2.2–2.4 V, are also observed, corresponding to the gradual oxidation of $Li_2S$ back to $S_8$. This process also involves polysulfide dissolution and a solid-phase nucleation step. However, unlike the discharge process, the oxidation during charging occurs more progressively, resulting in a smoother transition between the two plateaus [12–15]. Lithium polysulfides

* Corresponding authors.
*E-mail addresses:* m.oloomi@um.ac.ir (M. Oloomi-Buygi), acabot@irec.cat (A. Cabot).

https://doi.org/10.1016/j.est.2025.117023
Received 9 February 2025; Received in revised form 23 April 2025; Accepted 9 May 2025
Available online 28 May 2025

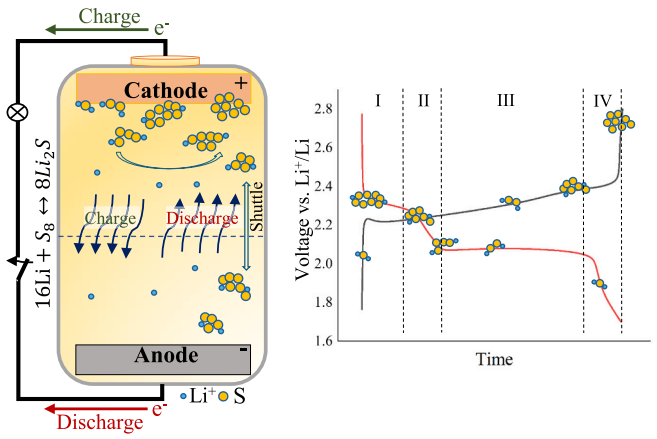


**Fig. 1.** Schematics of an LSB cell and its charge and discharge profiles.

(LiPSs) intermediates dissolved in the organic electrolyte can migrate to the anode side, leading to a loss of active material and a significant reduction in coulombic efficiency [16–18]. This migration, often referred to as the polysulfide shuttle effect, not only depletes the sulfur cathode but also causes parasitic reactions at the anode, further degrading overall battery performance and complicating its modelling [16,19,20].

Although computationally efficient, electric circuit models fail to capture the complex electrochemical phenomena in sulfur cathodes across diverse operating conditions [13,21,22]. In contrast, electrochemical models provide a robust framework for simulating battery behaviour and understanding the internal electrochemical kinetics and ion transport. These models should incorporate detailed descriptions of the battery's internal reactions, electrochemical kinetics, and charge transfer processes [23,24]. The success of a model-based approach relies on its capacity to replicate real battery behaviour and identify critical parameters essential for optimizing performance [21,24,25].

One-dimensional (1D) models capture both reaction kinetics and ion transport dynamics, offering a detailed representation of the system. However, their predictive applications are often limited by significant complexity and high computational costs [21,26]. In contrast, zero-dimensional (0D) models simplify the battery system by treating it as a single point without accounting for spatial variations in properties such as concentration, temperature, or potential within the battery volume. This simplicity enables 0D models to provide valuable insights into the kinetics of cathode reactions and phenomena like the shuttle effect while maintaining computational efficiency [26].

The first published 0D model for lithium-sulfur batteries (LSBs) was developed by Mikhaylik and Akridge [27], which focused on examining the relationship between the polysulfide shuttle effect and the current rate. Their model employed a two-step reaction process and accounted for heat generation resulting from the shuttle effect. Subsequently, Xu et al. [26] conducted a comparative study of four 0D models, each representing different sets of possible redox reactions in LSBs. Additionally, parameter identification and sensitivity analyses have been performed for various electrochemical models to evaluate the number of possible reaction pathways and identify the most critical parameters influencing battery performance.

Herein, we employ a 0D model adapted from the mathematical formulations proposed for the LSB electrochemical process in [21,26,28], with targeted modifications to capture key performance characteristics of typical LSBs while maintaining relatively low computational cost. Unlike the well-established two-step sulfur redox chain simplification [28], our model incorporates a more detailed three-step electrochemical reaction mechanism, explicitly including the polysulfide intermediate $S_6^{2-}$. This enhancement yields a discharge profile that better reflects experimental LSB behaviour, especially in the dip region, and enables more accurate modelling of shuttle effects and the evolution of intermediate species. To improve computational efficiency and solver stability, the Butler–Volmer equations are linearized, enabling the model to be efficiently solved as a system of differential-algebraic equations (DAEs). Additionally, high-order polysulfide shuttling and precipitation processes are modeled using constant shuttle and precipitation rates. Experimental data used for model validation were obtained from our previous work on LSB cells featuring a sulfur cathode composed of $Li_2S$ supported on Ketjen Black (KB) with embedded cobalt nanoparticles ($Li_2S$-Co@KB), which enhance electrochemical kinetics [3]. The modelling framework includes a scalable, physically informed parametrization strategy to ensure strong alignment between simulated results and real coin cell measurements. After validating the model under various conditions and conducting a sensitivity analysis, we performed parameter identification using an advanced optimization procedure. A key innovation lies in the parameterization strategy, where the objective function emphasizes not only the overall output error but also the timing and features of the dip region. To solve this complex optimization problem, we employ a combination of particle swarm optimization and a hybrid approach integrating global (Bayesian optimization) and local (Nelder–Mead simplex) techniques. This approach shows promise as it enables systematic exploration of different battery models and the parameterization of new experimental materials during the research phase.

The article is structured as follows: Section 2 outlines the model framework, methods for determining initial conditions, and parameter identification. Section 3 presents a simulation study examining the effects of shuttle and precipitation phenomena on discharge voltage performance and details the parameter identification process using experimental data. Finally, the findings of this work are summarized in Section 4.

## 2. Model

### 2.1. Model selection and improvement

0D models enable the simulation of complex electrochemical processes, such as the Li—S reaction at the cathode of LSBs, while maintaining low computational costs, which allows for the efficient screening of multiple parameters. These models have been demonstrated useful for the control and monitoring of the LSBs [26]. To accurately describe experimental electrochemical phenomena during LSB discharging, a three-step sulfur reduction mechanism is sufficient, striking a balance between computational simplicity and accuracy. The three-step model considered is described in Eqs. (1) to (3) [26].

$$\mathrm{H1}: \frac{3}{8}S_8 + e^- \rightleftharpoons \frac{1}{2}S_6^{2-} \tag{1}$$

$$\mathrm{H2}: S_6^{2-} + e^- \rightleftharpoons \frac{3}{2}S_4^{2-} \tag{2}$$

$$\mathrm{L}: \frac{1}{6}S_4^{2-} + e^- \rightleftharpoons \frac{2}{3}S^{2-} \tag{3}$$

Where H1, H2, and L represent the reactions that take place in different regions of the discharge profile. This model focuses exclusively on the sulfur reactions occurring at the cathode, neglecting the anode overpotential by assuming an unlimited supply of lithium on the anode side. In the third stage of the model, the liquid-phase $S^{2-}$ species are formed and subsequently precipitate as solid $S_p$ at approximately 2.1 V. The amount of precipitation is governed by the precipitation rate ($k_p$) and the saturated mass of $S^{2-}$ ($S_p^{2-}$) in the electrolyte. Additionally, the shuttle effect is incorporated into the model through the shuttle rate ($k_s$), which influences the mass evolution of dissolved polysulfide species during the high-voltage plateau [26]. Based on Faraday's first law of electrolysis and incorporating the shuttle effect, Eqs. (4) to (8) describe

**Table 1**
List of variables and parameters used in Eqs. (1)–(19).

| Symbol | Name | Units |
|---|---|---|
| $M_S$ | Sulfur molar mass ($S_8$) | g $mol^{-1}$ |
| $n_{Si}(i: 8, 6, 4, 1)$ | Number of sulfur atoms in LiPS | – |
| $n_e$ | Number of electrons per reaction | – |
| F | Faraday constant | C $mol^{-1}$ |
| R | Gas constant | J $K^{-1}$ $mol^{-1}$ |
| T | Temperature | K |
| $k_s$ | Shuttle rate | $s^{-1}$ |
| $k_p$ | Precipitation rate | $g^{-1}s^{-1}$ |
| $S_p^{2-}$ | Saturation mass of $S^{2-}$ | g |
| $E_i^0$ (i : H1, H2, L) | Standard potential | V |
| $I_i^0$ (i : H1, H2, L) | Current density | A $m^{-2}$ |
| I | Discharge current | A |
| $a_r$ | Reaction area | $m^2$ |
| $\nu$ | Electrolyte volume | L |
| $\eta_i$(i : H1, H2, L) | Overpotentials | V |
| $x_i$ (i:1–5) | Mass of sulfur species | g |
| V | Voltage | V |

the temporal evolution of sulfur species [26].

$$\dot{x_1} = -\frac{3}{8}\frac{n_{S8}M_S}{n_eF}I_{H1} - k_s x_1 \tag{4}$$

$$\dot{x_2} = \frac{1}{2}\frac{n_{S6}M_S}{n_eF}I_{H1} + k_s x_1 - k_s x_2 - \frac{n_{S6}M_S}{n_eF}I_{H2} \tag{5}$$

$$\dot{x_3} = \frac{3}{2}\frac{n_{S4}M_S}{n_eF}I_{H2} + k_s x_2 - \frac{1}{6}\frac{n_{S4}M_S}{n_eF}I_L \tag{6}$$

$$\dot{x_4} = \frac{2}{3}\frac{n_S M_S}{n_eF}I_L - k_p x_5\left(x_4 - S_p^{2-}\right) \tag{7}$$

$$\dot{x_5} = k_p x_5\left(x_4 - S_p^{2-}\right) \tag{8}$$

where $x_1$, $x_2$, $x_3$, $x_4$ and $x_5$ represent the mass of sulfur species $S_8$, $S_6^{2-}$, $S_4^{2-}$, $S^{2-}$, and $S_p$ respectively, $\dot{x}$ represents $\frac{dx}{dt}$, and other variables and parameters of (4)–(8) are defined in Table 1. The term $k_s x_i$ in (4)–(6) indicates the shuttle effect on the mass changes of high-order polysulfides. Similar to the polysulfide shuttling, the precipitation process is modeled by the constant rate $k_p$ in Eqs. (7) and (8).

The Nernst Eqs. (9)–(11) are employed to calculate the equilibrium potential of reactions [26].

$$E_{H1} = E_{H1}^0 - \frac{RT}{F}\left(-\frac{3}{8}\ln\left(\frac{x_1}{n_{S8}M_S\nu}\right) + \frac{1}{2}\ln\left(\frac{x_2}{n_{S6}M_S\nu}\right)\right) \tag{9}$$

$$E_{H2} = E_{H2}^0 - \frac{RT}{F}\left(-\ln\left(\frac{x_2}{n_{S6}M_S\nu}\right) + \frac{3}{2}\ln\left(\frac{x_3}{n_{S4}M_S\nu}\right)\right) \tag{10}$$

$$E_L = E_L^0 - \frac{RT}{F}\left(-\frac{1}{6}\ln\left(\frac{x_3}{n_{S4}M_S\nu}\right) + \frac{2}{3}\ln\left(\frac{x_4}{n_S M_S\nu}\right)\right) \tag{11}$$

Where variables and parameters of (9)–(11) are defined in Table 1.

The reaction currents in the three-step electrochemical process are described by the Butler-Volmer equations. These equations detail the relationship between the reaction currents at the electrode-electrolyte interface and the overpotentials. The general form of this equation is as follows:

$$I = I^0\left[\exp\left(\frac{\beta F}{RT}\eta\right) - \exp\left(-\frac{(1-\beta)F}{RT}\eta\right)\right] \tag{12}$$

where β is known as the symmetry factor or charge transfer coefficient. The value of β is usually considered to be 0.5, which implies that the transition state is located midway along the reaction pathway and that the activation energy distribution between the oxidation and reduction steps is symmetric [29]. Assuming β = 0.5, the Butler-Volmer equations are expressed as follows:

$$I_{H1} = 2I_{H1}^0 a_r \sinh\left(\frac{n_eF\eta_{H1}}{2RT}\right) \tag{13}$$

$$I_{H2} = 2I_{H2}^0 a_r \sinh\left(\frac{n_eF\eta_{H2}}{2RT}\right) \tag{14}$$

$$I_L = 2I_L^0 a_r \sinh\left(\frac{n_eF\eta_L}{2RT}\right) \tag{15}$$

Where variables and parameters of (13)–(15) are defined in Table 1.

The driving force for initiating the reaction on the cathode side is a non-zero potential excess (overpotential), calculated as the difference between the Nernst potential and the cell voltage (V) [26].

$$\eta_{H1} = V - E_{H1} \tag{16}$$

$$\eta_{H2} = V - E_{H2} \tag{17}$$

$$\eta_L = V - E_L \tag{18}$$

The conservation of charge dictates that relation (19) holds.

$$I = I_{H1} + I_{H2} + I_L \tag{19}$$

The model thus defines a system of DAEs comprising 5 differential equations, specifically Eqs. (4)–(8), and 10 algebraic equations, namely Eqs. (9)–(11) and (13)–(19), as outlined in (20).

$$f(t, x, \dot{x}) = 0 \tag{20}$$

The system includes 15 variables, 5 differential ($x_i$, for i: 1–5) and 10 algebraic:

$$x = [x_1, x_2, x_3, x_4, x_5, I_{H1}, I_{H2}, I_L, V, \eta_{H1}, \eta_{H2}, \eta_L, E_{H1}, E_{H2}, E_L]^T \tag{21}$$

To simplify the model, $\sinh\left(\frac{n_eF\eta_i}{2RT}\right)$ is replaced by its linear approximation, i.e. $\frac{n_eF\eta_i}{2RT}$, in Eqs. (13) to (15). This approximation is valid for LSBs, as the reactions typically occur at low voltages and small deviations from equilibrium. This simplification enhances computational efficiency and ensures better stability and convergence of the numerical solver.

Generally, the first step in estimating the state parameters involves numerically solving the system of equations and comparing the output to experimental data. However, this system of equations poses challenges for numerical solutions due to instabilities that arise when state variables approach zero. To address this, non-zero initial conditions for the low-order polysulfides are required. Since the model involves 5 differential equations, 5 initial conditions must be specified to solve the system. It is assumed that the initial values of the voltage, the mass of sulfur ($x_1$), and the mass of precipitated sulfur ($x_5$) are known. Additionally, the initial value of $I_{H1}$ is assumed to be equal to the discharge current, and $I_L$ is considered to be zero. The initial condition for $I_{H2}$ is obtained from Eq. (19), while $\eta_i$ (for i:H1, H2, L) is calculated from (13) to (15), $E_i$ from Eqs. (16) to (18), and $x_2$, $x_3$, and $x_4$ from Eqs. (9) to (11). Assuming that the constant parameters of the 0D model are known, i.e. $E_i^0$, $I_i^0$, $k_p$, $k_s$, $a_r$, $\nu$, m and I, and that the initial conditions are provided, the 0D model can be solved. In this study, the system of DAEs is solved using the implicit Newton-Raphson method, which ensures robustness and convergence [30].

### 2.2. Experimental parametrization: bridging experimental data and model development

The LSB cells assembled and tested to validate the model consist of a $Li_2S$-Co@KB cathode, a lithium metal anode, and an ether-based electrolyte. The $Li_2S$-Co@KB cathode, developed based on our previous

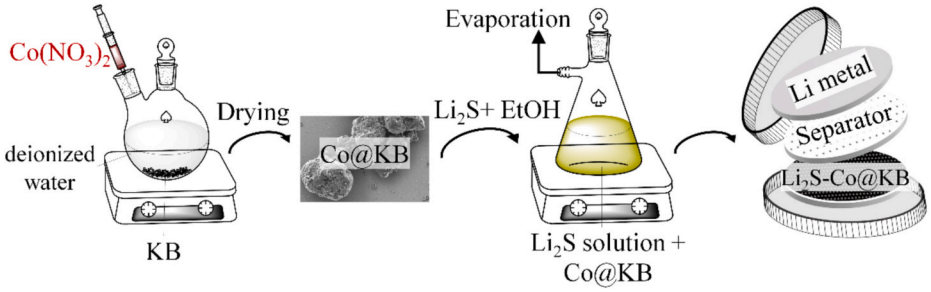


**Fig. 2.** Schematic of $Li_2S$-Co@KB coin cell assembly.

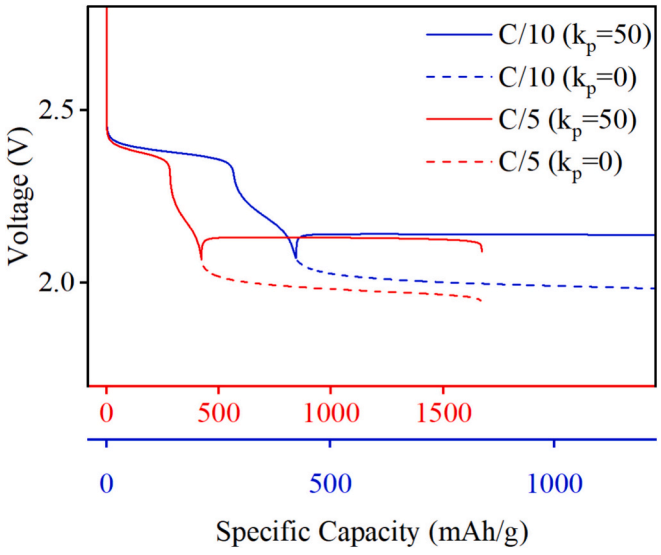


**Fig. 3.** Simulated galvanostatic discharge curves at two different currents and precipitation rates.

work [3], comprises $Li_2S$ as the active material supported on high-surface-area, highly conductive KB carbon, with cobalt nanoparticles added as a catalytic additive to enhance the Li—S reaction. The ether-based electrolyte is a solution containing 0.1 M LiTFSI, 1,2-dimethoxyethane (DME), 1,3-dioxolane (DOL) (*v*/v = 1:1), and 0.2 M $LiNO_3$. To fabricate the cathode, the $Li_2S$-Co@KB composite was mixed with PVDF and conductive carbon in an 8:1:1 weight ratio. The resulting slurry was cast onto aluminium foil, dried at 100 °C inside a glovebox, and punched into 12-mm discs to serve as the cathode. The assembled batteries were tested using a Neware BTS4008 battery tester. For initial activation, the batteries underwent one cycle at a 0.1C current rate, and the subsequent discharge profile was used for modelling. A schematic representation of the cell preparation process, from material synthesis to coin cell assembly, is provided in Fig. 2.

Since the coin cell data are small-scale and not directly suitable for modelling, scaling between the real sample and the simulation is required. To achieve this, as outlined in reference [26], the model current is assumed to be proportional to the actual battery current, scaled by a constant factor c, i.e. $I_{model} = c \times I_{bat.}$. This scaling factor is then used to determine the coefficients for other parameters, including mass, length, $a_r$, $\nu$, $I_i^0$, and $k_p$ that are equal to c, $c^{\frac{1}{3}}$, $c^{\frac{2}{3}}$, c, $c^{\frac{1}{3}}$, and $\frac{1}{c}$ respectively. These coefficients were incorporated into the model for the simulation process. In LSBs, the solubility of $Li_2S$ in ether-based electrolytes is very low [31,32]. Therefore, for this model, the saturation mass of $S^{2-}$ is assumed to be 0.0001 (g) [26]. Additionally, the electrolyte volume used during cell assembly was 10 μL, and after scaling, it was adjusted to 0.012 L per cell. These assumptions ensure that the model reflects realistic conditions while maintaining computational simplicity.

### 2.3. Parameter identification

To estimate the parameters $I_i^0, k_p, k_s, m$ and $E_i^0$ in the proposed 0D model, an optimization problem is formulated to ensure that the simulated voltage ($V_{sim}$) closely matches the experimental voltage ($V_{exp}$). The objective function is defined as the squared norm of the difference between $V_{exp}$ and $V_{sim}$, with particular emphasis on accurately capturing the dip point in the discharge curve, which represents the transition between the first and second flat regions. The equations governing the behaviour of the LSB are included as constraints in the optimization problem. By assigning weights to the error across different regions of the curve, the optimization prioritizes preserving the voltage dynamics in both flat regions and around the dip point. Additionally, the time of occurrence of the voltage dip point is included in the objective function

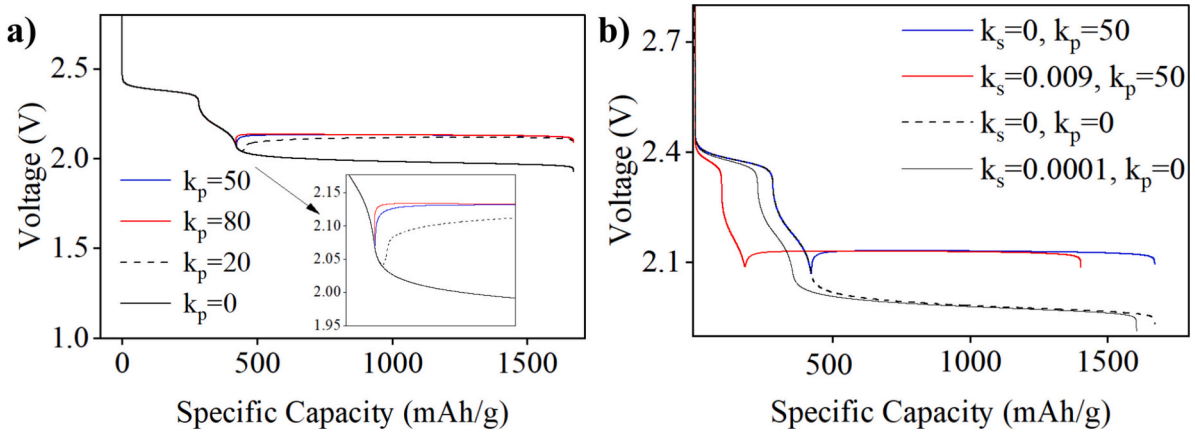


**Fig. 4.** a) Effects of precipitation on discharge curve. b) Effects of the LiPS shuttle on the discharge curve.

to ensure the model accurately reflects not only the voltage values but also their temporal evolution. The proposed optimization formulation for parameter identification is detailed in Eqs. (22) to (39).

Where N is the total number of experimental data points, $w_{dip}$ is the weight assigned to the dip point region, emphasizing its importance, and $w_{other}$ is the weight for the remaining regions of the curve. $V_{exp.,dip}$ and $V_{sim.,dip}$ are the experimental and simulated voltage values, respectively, within the dip region. $V_{exp.,other}$ and $V_{sim.,other}$ are the experimental and simulated voltage values outside the dip region. Additionally, $w_{dip\_time}$ represents the weight assigned to the time of occurrence of the dip point, ensuring that the temporal accuracy of the model is also prioritized. To identify the dip point region, the lowest value of voltage in the first half of the experimental/simulated data is considered as the centre or dip point of the experimental/simulated data. A predefined range is then established around this centre to capture the dip point region.

constraints, comprising the DAEs described in Eqs. (23) to (39), are solved using the implicit Newton-Raphson method. After solving the DAEs, the voltage curve is extracted, and the objective function or fitness, defined in Eq. (22), is computed. This process is repeated across multiple generations of particles, with the particles iteratively adjusted to converge on the optimal solution. Through these iterations, the PSO method seeks to identify the optimal values for the 9 parameters specified in Eq. (38). However, the PSO method was not successful in all runs, and some runs failed to converge, leading to inconsistent results. As a result, an alternative approach was sought.

### 2.4.2. BO-NMS method

To overcome the limitations of PSO, the BO-NMS hybrid optimization method was employed. This method combines probabilistic (BO) and heuristic (NMS) approaches, leveraging the strengths of both. BO provides a probabilistic framework to explore the parameter space efficiently, while NMS refines the solution by performing local search

$$\mathbf{Min}_z J = \mathbf{s.t.}: \sqrt{\frac{1}{N}\left(w_{dip}\left\|V_{exp.,dip}-V_{sim.,dip}\right\|_2^2 + w_{other}\left\|V_{exp.,other}-V_{sim.,other}\right\|_2^2\right)} + w_{dip,time}\times\left|t_{exp,dip}-t_{sim,dip}\right| \quad (22)$$

**s.t.:**

$$\dot{x_1}(t) = -\frac{3}{8}\frac{n_{S8}M_S}{n_eF}x_6(t) - k_s x_1(t) \quad (23)$$

$$\dot{x_2}(t) = \frac{1}{2}\frac{n_{S6}M_S}{n_eF}x_6(t) + k_s x_1(t) - k_s x_2(t) - \frac{n_{S6}M_S}{n_eF}x_7(t) \quad (24)$$

$$\dot{x_3}(t) = \frac{3}{2}\frac{n_{S4}M_S}{n_eF}x_7(t) + k_s x_2(t) - \frac{1}{6}\frac{n_{S4}M_S}{n_eF}x_8(t) \quad (25)$$

$$\dot{x_4}(t) = \frac{2}{3}\frac{n_SM_S}{n_eF}x_8(t) - k_p x_5(t)\left(x_4(t) - S_p^{2-}\right) \quad (26)$$

$$\dot{x_5}(t) = k_p x_5(t)\left(x_4(t) - S_p^{2-}\right) \quad (27)$$

$$x_6(t) = 2I_{H1}^0 a_r\left(\frac{n_eFx_{10}(t)}{2RT}\right) \quad t=1,2,3,\ldots,N \quad (28)$$

$$x_7(t) = 2I_{H2}^0 a_r\left(\frac{n_eFx_{11}(t)}{2RT}\right) \quad t=1,2,3,\ldots,N \quad (29)$$

$$x_8(t) = 2I_L^0 a_r\left(\frac{n_eFx_{12}(t)}{2RT}\right) \quad t=1,2,3,\ldots,N \quad (30)$$

$$x_{10}(t) = x_9(t) - x_{13}(t) \quad t=1,2,3,\ldots,N \quad (31)$$

$$x_{11}(t) = x_9(t) - x_{14}(t) \quad t=1,2,3,\ldots,N \quad (32)$$

$$x_{12}(t) = x_9(t) - x_{15}(t) \quad t=1,2,3,\ldots,N \quad (33)$$

$$x_{13}(t) = E_{H1}^0 - \frac{RT}{F}\left(-\frac{3}{8}\ln\left(\frac{x_1(t)}{n_{S8}M_S\nu}\right) + \frac{1}{2}\ln\left(\frac{x_2(t)}{n_{S6}M_S\nu}\right)\right) \quad t=1,2,3,\ldots,N \quad (34)$$

$$x_{14}(t) = E_{H2}^0 - \frac{RT}{F}\left(-\ln\left(\frac{x_2(t)}{n_{S6}M_S\nu}\right) + \frac{3}{2}\ln\left(\frac{x_3(t)}{n_{S4}M_S\nu}\right)\right) \quad t=1,2,3,\ldots,N \quad (35)$$

$$x_{15}(t) = E_L^0 - \frac{RT}{F}\left(-\frac{1}{6}\ln\left(\frac{x_3(t)}{n_{S4}M_S\nu}\right) + \frac{2}{3}\ln\left(\frac{x_4(t)}{n_SM_S\nu}\right)\right) \quad t=1,2,3,\ldots,N \quad (36)$$

$$I = x_6(t) + x_7(t) + x_8(t) \quad t=1,2,3,\ldots,N \quad (37)$$

$$z = \left[E_i^0, I_i^0, k_p, k_s, m\right] \quad i = H1, H2, L \quad (38)$$

$$\mathrm{x(t)}=[\mathrm{S_8(t)}, \mathrm{S_6^{2-}(t)}, \mathrm{S_4^{2-}(t)}, \mathrm{S^{2-}(t)}, \mathrm{S_p(t)}, \mathrm{I_{H1}(t)}, \mathrm{I_{H2}(t)}, \mathrm{I_L(t)}, \mathrm{V(t)}, \eta_{H1}(t), \eta_{H2}(t), \eta_L(t), \mathrm{E_{H1}(t)}, \mathrm{E_{H2}(t)}, \mathrm{E_L(t)}]^T \quad t=1,2,3,\ldots,N \quad (39)$$

## 2.4. Solving methods

The optimization process for the model involves solving a complex problem constrained by numerous nonlinear differential and algebraic equations. To address this, two methods have been employed: (a) the Particle Swarm Optimization (PSO) method and (b) the hybrid Bayesian Optimization-Nelder-Mead Simplex (BO-NMS) method. Each method is detailed below.

### 2.4.1. PSO method

The PSO method operates by generating a population of candidate solutions, referred to as particles. These particles are evaluated and iteratively improved by moving through the search space based on their own best-known positions and the swarm's collective best-known position. The process continues until a satisfactory solution is identified [33]. Each particle represents a set of specific values for the 9 unknown parameters defined in Eq. (38). To evaluate a particle, the optimization

optimizations. As with the PSO method, the unknown parameters are determined iteratively in the BO-NMS method. For each iteration, the DAEs of the 0D model are solved using the implicit Newton-Raphson method to compute the objective function. By alternating between global exploration and local refinement, the BO-NMS method effectively identifies the optimal solution, ensuring greater stability and convergence compared to PSO.

More in detail, BO is an advanced method for solving complex optimization problems without requiring gradient information. It works by approximating the objective function using probabilistic surrogate models, such as Gaussian processes, which are based on an initial sampling of data. A learning function is then used to intelligently select new points for evaluation. This acquisition function balances exploration, where unknown points are examined to improve knowledge about the objective function, and exploitation, which focuses on regions likely to provide the best value [34]. BO performs effectively in continuous domains with fewer than 20 dimensions and is robust against random noise

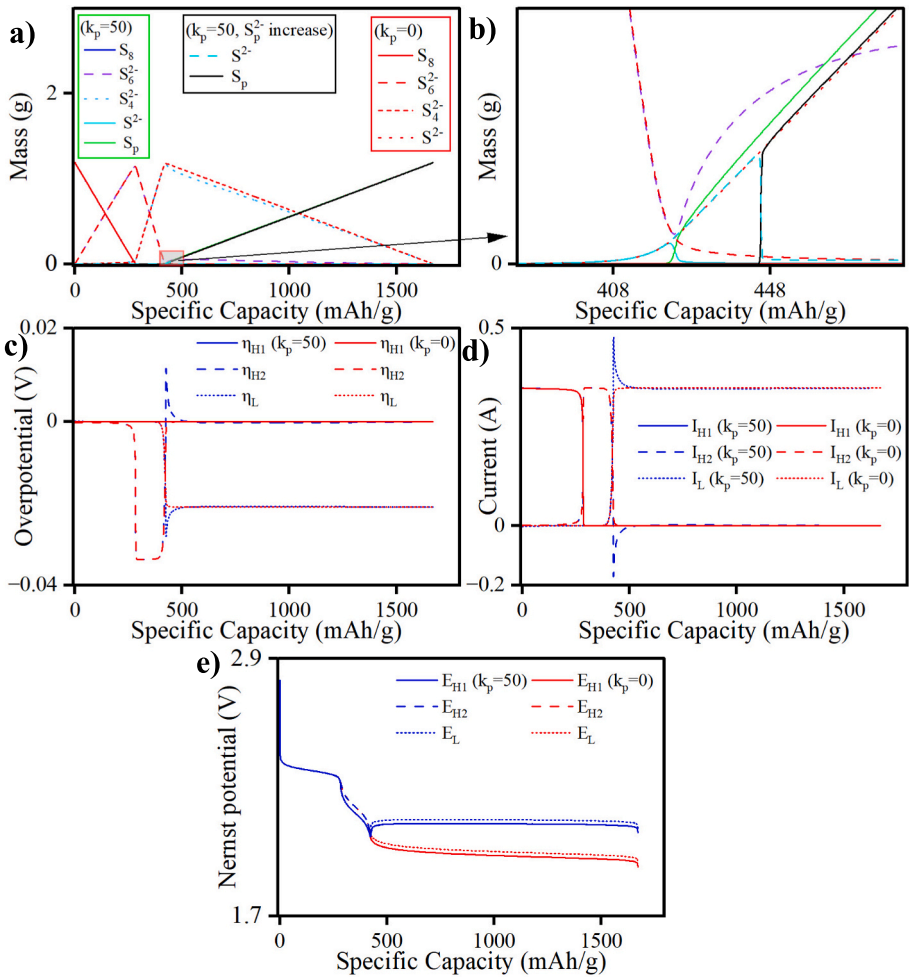


**Fig. 5.** Simulation of LSB variables during the discharge process, (a) Mass of sulfur species. (b) Mass of sulfur species over a portion of the time interval. (c) Overpotentials. (d) Reaction currents. (e) Nernst potentials.

in the evaluations of the objective function [35]. The process is iterative, with the probabilistic model being updated after each evaluation, providing increasingly accurate estimates of the objective function.

The NMS algorithm, on the other hand, is a local heuristic search method that optimizes functions without requiring derivatives or gradients. At its core, the algorithm uses a simplex, a geometric structure with n + 1 vertices in n-dimensional space, which moves and scales iteratively to locate the minimum of the objective function [36,37]. NMS converges quickly with relatively few evaluations of the objective function. However, its performance is highly dependent on the initialization of the simplex. Poor initialization can hinder search efficiency, making accurate initialization critical. In this study, BO is used to provide an appropriate starting point for the NMS algorithm, ensuring effective convergence.

To combine the strengths of BO and NMS, a hybrid optimization approach is employed. BO is applied iteratively, beginning with a high exploration ratio to thoroughly investigate the parameter space. As the optimization progresses, the exploration ratio is reduced, allowing the algorithm to focus on promising regions and refine the search for optimal points. In this study, BO was run twice using MATLAB, with a stopping criterion of 100 iterations for each run.

The results obtained from BO are then refined using the NMS algorithm. By initializing NMS with the near-optimal solution from BO, the algorithm starts close to the global optimum and can efficiently focus on smaller regions of the parameter space. The stopping criterion for NMS is set such that the algorithm halts if the change in the objective function value between two consecutive iterations is $<10^{-6}$. MATLAB's fminsearch function is used to implement the NMS algorithm.

This hybrid approach combines the global search capability of BO with the localized refinement of NMS. BO ensures that the search begins in a promising region, while NMS quickly minimizes the error within that region, providing a robust and efficient solution to the parameter identification problem.

## 3. Results and discussions

### 3.1. Investigating the shuttle and precipitation effects using a zero-dimensional model

In this section, the behaviour of the model is examined by solving the DAEs while keeping the values of $I^0_{H1}$, $I^0_{H2}$, $I^0_L$, $E^0_{H1}$, $E^0_{H2}$, $E^0_L$, and m constant, and varying $k_p$, $k_s$, and I. Fig. 3 illustrates the simulation results of battery voltage during discharge at C/5 and C/10 rates, using two different values of $k_p$ and assuming a theoretical capacity of 1675 mAh/g. It should be mentioned that the presented model does not take into account mass transport limitations that arise at higher C-rates. In real LSBs, mass transport limitations lead to reduced sulfur utilization and premature discharge termination due to concentration gradients within the electrolyte and cathode. These additional spatial effects of mass transport limitations are not considered in the 0D model, which assumes uniform species distribution. As a result, the model represents the fresh cell behaviour under idealized well-mixed conditions without attempting to predict capacity loss due to C-rate. Discharge simulations are performed to a predetermined initial sulfur mass, and the

voltage–capacity profiles are used to qualitatively illustrate the impact of C-rate variation on discharge profiles. It should also be noted that both voltage profiles in Fig. 3, depict the theoretical capacity of the cell based on complete utilization of the initial sulfur mass.

As shown in Fig. 3, the voltages of the two typical plateaus in the discharge curve decrease as the discharge current increases. This behaviour arises from intrinsic physical limitations and unavoidable losses associated with diffusion and charge transfer reactions, which constrain the cell's ability to deliver power. During discharge, ions must diffuse through the electrolyte to the electrode surfaces. At higher discharge currents, ions must diffuse faster to sustain the reaction. However, when the ion diffusion rate cannot keep up with the current demand, the reaction sites are inadequately supplied, causing a voltage drop in the cell. Additionally, the reaction kinetics, governed by the Butler-Volmer equation, play a crucial role in controlling charge transfer between the electrolyte and the electrode materials where the electrochemical reactions occur. At higher discharge currents, the reaction overpotential, i.e. the additional voltage required to drive the reaction at a given rate, increases proportionally. This overpotential reflects an extra energy loss, further reducing the overall voltage of the cell. Together, these diffusion and reaction kinetics effects explain the observed voltage drop at higher discharge currents.

The dashed blue and black curves in Fig. 3 demonstrate that in the absence of precipitation ($k_p = 0$), the voltage level of the upper plateau remains unchanged. When precipitation is included in the model, all its features become apparent, including the pronounced impact of precipitation on the discharge voltage curves. Precipitated lithium sulfide can obstruct the discharge process in LSBs and significantly influences the internal resistance and voltage profile of the cell, particularly affecting the shape of the discharge curve in the lower voltage plateau. Precipitation directly contributes to both a voltage increase in the low plateau and the emergence of the dip point between the two plateaus. The dip point represents a sharp transition between two distinct sets of redox processes occurring during the discharge of the LSB [38].

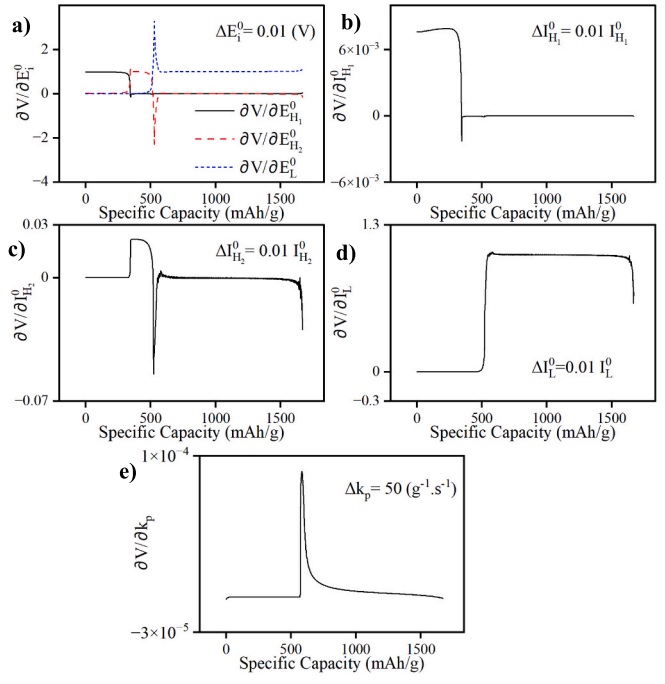


**Fig. 6.** (a) Voltage sensitivity to the standard reduction potentials $E_{H1}^0$, $E_{H2}^0$, and $E_L^0$. (b) Voltage sensitivity to the exchange current density $I_{H1}^0$. (c) Voltage sensitivity to the exchange current density $I_{H2}^0$. (d) Voltage sensitivity to the exchange current density $I_L^0$. (e) Voltage sensitivity to the precipitation rate constant $k_p$.

**Table 2**
Parameters estimated at two discharge current rates of 0.2C and 0.5C.

| Predicted parameters | Values estimated by PSO @ 0.2C | Values estimated by BO-NMS @ 0.2C | Values estimated by BO-NMS @ 0.5C |
|---|---|---|---|
| $E_{H1}^0$(V) | 2.364 | 2.361 | 2.359 |
| $E_{H2}^0$(V) | 2.257 | 2.257 | 2.200 |
| $E_L^0$(V) | 2.105 | 2.104 | 2.054 |
| $I_{H1}^0$(A/m$^2$) | 14.736 | 14.736 | 18.421 |
| $I_{H2}^0$(A/m$^2$) | 3.728 | 3.669 | 9.210 |
| $I_L^0$(A/m$^2$) | 0.434 | 0.442 | 1.602 |
| $k_p$ ($g^{-1}.s^{-1}$) | 23 | 32 | 140 |
| $k_s$ ($s^{-1}$) | 0.000105 | 0.000108 | 0.0001 |
| m (g) | 0.001059 | 0.001062 | 0.001099 |

The impact of varying $k_p$ on the voltage curve with constant current and constant $k_s$ is clearly illustrated in Fig. 4a. This figure shows that changes in $k_p$ specifically impact the second flat region of the voltage curve, while the first flat region remains unaffected, which aligns with findings reported in the literature [39]. In Fig. 4b, the effect of varying $k_s$ is analyzed at a constant current rate for two different values of $k_p$. At a fixed $k_p$, the voltage level of the second flat region remains unchanged regardless of variations in $k_s$. However, the voltage level of the first flat region is influenced by $k_s$, as highlighted by the blue and red curves, as well as the solid and dashed black lines.

As observed in Fig. 4b, and consistent with the model proposed by Mikhaylik and Akridge [27], $k_s$ acts as a scaling factor for the voltage response of the cell under constant precipitation and current rate conditions. The results presented in Fig. 3 and Fig. 4 further reveal that in the absence of precipitation ($k_p = 0$), the discharge current and the shuttle effect primarily influence the battery behaviour [27]. Conversely, in the absence of the shuttle effect ($k_s = 0$), the discharge current and $k_p$ affect the battery voltage response. Since both precipitation and the shuttle effect are typically present during discharge, the current, $k_s$ and $k_p$ collectively define the performance of a real LSB. Specifically, the discharge voltage at the upper plateau is primarily governed by the current and $k_s$, while the discharge voltage at the lower plateau is determined by the current and $k_p$.

Fig. 5 provides a detailed comparison of the changes in the mass of sulfur species, overpotentials, reaction currents, and Nernst potentials over time for three different scenarios: 1) $k_p = 50$, representing a high precipitation rate; 2) $k_p = 0$, representing no precipitation; and 3) a scenario where $S_p^{2-}$ increases under $k_p = 50$, reflecting a rise in the saturation limit of $S^{2-}$ in the electrolyte.

As expected, at the beginning of the discharge process, $S_8$ is sequentially consumed and converted into $S_6^{2-}$, then $S_4^{2-}$, followed by $S^{2-}$, and finally precipitates as $S_p$ ($Li_2S$) when $k_p > 0$. In contrast, when $k_p = 0$, the final discharge product remains as $S^{2-}$, with no $Li_2S$ precipitation (Fig. 5a,b). The parameter $S_p^{2-}$ determines the onset of precipitate formation and influences both the timing and the amount of precipitate formed during discharge. Higher values of $S_p^{2-}$ at $k_p = 50$ result in a delayed onset of $Li_2S$ precipitation.

Fig. 5c and d show the variations in overpotentials and reaction currents, respectively. The overpotential $\eta_{H1}$ remains constant regardless of changes in $k_p$. However, $\eta_{H2}$ and $\eta_L$ exhibit a sharp change around the voltage dip point, which becomes more pronounced with higher $k_p$. Similarly, the reaction currents $I_{H2}$ and $I_L$ show significant peaks at $k_p = 50$, whereas $I_{H1}$ remains unaffected.

Fig. 5e presents the variations in the Nernst potentials $E_{H1}$, $E_{H2}$ and $E_L$. These potentials differ from the battery terminal voltage at any given time by the amount of their corresponding overpotentials. The voltage dip point marks the onset of $Li_2S$ precipitation [38], and occurs approximately 5000 s after the start of discharge, coinciding with the observed increase in $S_p$.

It should be noted that the predicted discharge curve deviates

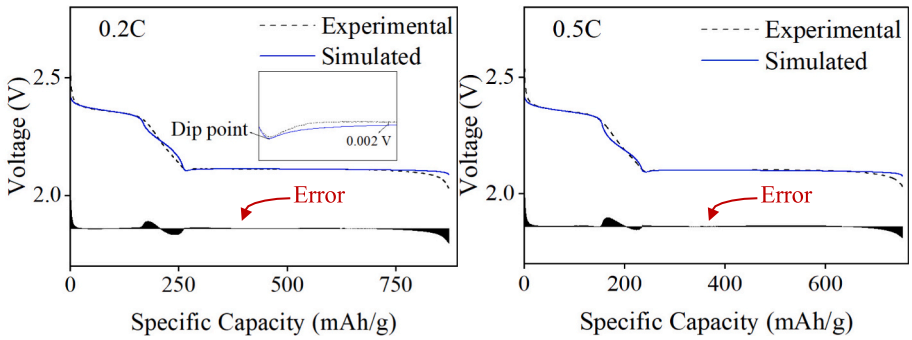


**Fig. 7.** Comparison of the experimental discharge curves of a $Li_2S$-Co@KB-based cell and the simulated discharge curve using parameters estimated through BO-NMS optimization at 0.2C (left) and 0.5C (right).

slightly from the actual behaviour of LSBs. For instance, at the end of the upper flat plateau, the model exhibits a steep voltage drop that is less pronounced in real LSBs. This discrepancy may be attributed to the reduced number of reaction steps included in the model. In this study, a three-step reaction mechanism is considered, which could be refined by increasing the number of steps in the sulfur conversion process to capture more detailed dynamics. Additionally, the model only accounts for the precipitation of the lowest-order LiPS species, represented by $2Li^+ + S^{2-} \rightleftharpoons Li_2S$. By incorporating more comprehensive precipitation models, the accuracy of the model in simulating the lower flat region of the voltage curve could be significantly improved. Despite these limitations, the proposed 0D model demonstrates a good approximation of the key electrochemical processes occurring in LSBs. In the following section, the parameters of the fabricated battery are estimated to further validate the model's accuracy.

### 3.2. Sensitivity analysis of different parameters

To further analyze the contributions of different parameters to the overall shape of the voltage curve, a sensitivity analysis was conducted involving varying one parameter at a time and calculating the partial derivatives of voltage with respect to selected thermodynamic and kinetic parameters [26]. The results are shown in Fig. 6.

Fig. 6a displays the sensitivity of voltage to the equilibrium potentials $E^0_{H1}$, $E^0_{H2}$, and $E^0_L$. The results indicate that the voltage profile is affected by $E^0_{H1}$ firstly, where the high-voltage redox reactions are most active. After that $E^0_{H2}$ affect the voltage up to the dip point region. Conversely, $E^0_L$ is only effective to the latter part of the discharge, where the voltage transitions into the lower voltage plateau. Thus, it is evident that accurate parameterization of equilibrium potentials is significant, especially with regard to the two-plateau behaviour of LSBs.

Fig. 6b shows that voltage sensitivity to $I^0_{H1}$ was most pronounced during the early discharge period. Meanwhile, the voltage sensitivity to the $I^0_{H2}$ illustrated in Fig. 6c shows a more complex pattern, as it retains considerable sensitivity throughout the dip point region. The voltage sensitivity to the $I^0_L$ illustrated in Fig. 6d, shows a steep jump in sensitivity, as the cell begins to enter the lower voltage plateau and maintain a high influence until full discharge. This emphasizes that measuring low-voltage kinetics correctly is critical to effectively model the behaviour of the cell as it approaches the end-of-discharge.

Finally, Fig. 6e shows voltage sensitivity with respect to the precipitation rate constant $k_p$. A peak appeared around the dip point region, but is quickly diminished suggesting a less critical role in the later stages of discharge.

Overall, each parameter demonstrates dominance within specific capacity ranges, reinforcing the physical consistency of the model and highlighting the necessity of precise calibration to accurately capture system behaviour across diverse operating conditions. This analysis also underscores the inherent limitations of the 0D modelling framework, which omits spatial effects such as mass transport and diffusion constraints. These factors, while neglected here for computational efficiency, can significantly influence parameter sensitivities in real systems and should be considered in higher-dimensional modelling approaches.

### 3.3. Experimental parametrization

The parameters of the 0D model were estimated using both the PSO and the hybrid BO-NMS methods for two discharge current rates of 0.2C and 0.5C. Table 2 presents the parameters estimated using the BO-NMS optimization method, which provided more consistent and reliable results, alongside the best results obtained from several PSO runs.

PSO is effective for non-convex optimization problems and does not rely on gradient information. However, in this study, PSO often faced challenges in adequately exploring the search space and adjusting parameters effectively in regions with significant variations. Furthermore, PSO required substantially more computational time, up to three times longer than the hybrid BO-NMS method, to achieve comparable results. In contrast, BO-NMS proved to be more robust and computationally efficient. By combining the strengths of probabilistic exploration, strategic exploitation, and precise local refinement, BO-NMS achieved a better balance across the optimization process. This balance allowed it to converge to optimal solutions more reliably and with a significantly lower computational burden compared to PSO, making it a more effective approach for parameter estimation in this study.

Fig. 7 compares the experimental discharge curves of the $Li_2S$-Co@KB-based cell with the simulated curves generated using the BO-NMS estimated parameters at two different current rates. The 0D model successfully reproduces the key features of the discharge behaviour, including the voltage dip point and the flat regions at both current rates. The simulated voltage closely aligns with the measured voltage dynamics, demonstrating the accuracy of the model. Additionally, the root-mean-square error (RMSE) between the simulated and experimental voltages is approximately 10 mV for both graphs over the measured points, indicating a high level of precision in capturing the battery's discharge characteristics.

The error bars shown at the bottom of Fig. 7 highlight greater deviations in the slope transition region between the high and low voltage plateaus. This error is attributed to the use of simplified Butler-Volmer equations, which assume that the concentrations of reactants and products remain constant and do not directly affect the current. However, near the dip point, where transitions between phases occur, concentration gradients can form due to precipitation or accumulation of species. In real electrochemical systems, the current is influenced not only by the overpotential but also by the concentrations of reactants and products at the electrode surface. To explicitly account for the dependence of the Butler-Volmer equation on the concentrations of sulfur species (as in Eqs. (13) to (15)), the exchange current density can be modified to include the actual concentrations of species at the electrode surface [21]. While this modification provides a more accurate

representation of the electrochemical processes, it also increases the model's sensitivity to initial conditions and significantly adds to the computational burden. Since the parameters identified using the simplified Butler-Volmer equations closely match experimental values and the key characteristics of the voltage curve are accurately captured, this error has been deemed acceptable and ignored in the current study.

Fig. 8 displays the weight changes of different sulfur species, reaction currents, overpotentials, and Nernst potentials at a discharge current rate of 0.2C. A comparison of the parameters estimated using the BONMS method at two different current rates is summarized in Table 2. The results reveal that at 0.5C, compared to 0.2C, the parameters $E^0_{H1}$, $E^0_{H2}$, and $E^0_L$ decrease slightly, reflecting an increase in polarization effects and a larger deviation from equilibrium conditions. Among these, $E^0_{H2}$ exhibited the most significant reduction, dropping from 2.257 V to 2.200 V. This suggests that the intermediate polysulfide species ($S_6^{2-}$) faces the greatest difficulty in maintaining equilibrium as the discharge rate increases, highlighting the thermodynamic challenges associated with operating LSBs at higher current rates.

As shown in Table 2, the parameters $I^0_{H1}$, $I^0_{H2}$, and $I^0_L$ increase at higher discharge rates, indicating that faster kinetics are required to support the higher discharge rates. $I^0_{H1}$ rises from 14.736 to 18.421 A/m$^2$, highlighting the critical role of the early-stage polysulfide reduction ($S_8 \rightarrow S_6^{2-}$) in enabling the system to adapt to increased current demands. The subsequent increases in $I^0_{H2}$ and $I^0_L$ confirm that kinetic enhancements occur in the intermediate and late stages of discharge, supporting the overall performance of the battery under higher current conditions.

When the current rate is increased from 0.2C to 0.5C, $k_p$ rises from 32 to 140 $g^{-1}s^{-1}$, while $k_s$ decreases from $1.08 \times 10^{-4}$ to $1.0 \times 10^{-4}$ $s^{-1}$, indicating a significant reduction of the shuttle effect at the higher current rate.

This reduction can be explained by several factors: i) The faster reduction of dissolved polysulfides at the cathode during discharge leaves less material available to diffuse toward the anode; ii) The increase in $k_p$ accelerates the precipitation of solid-phase products, such as $Li_2S$, which reduces the concentration of soluble polysulfides in the electrolyte and limits their mobility; iii) The shorter discharge time associated with higher current rates decreases the time available for polysulfides to diffuse to the anode, further suppressing the shuttle effect.

The increase in $k_p$ reflects the system's ability to adapt to high current rates by facilitating the rapid conversion of dissolved polysulfides into solid products. However, this adaptation can come at a cost, as more rapid precipitation may occur inhomogeneously, potentially passivating the electrodes and reducing the utilization of active material.

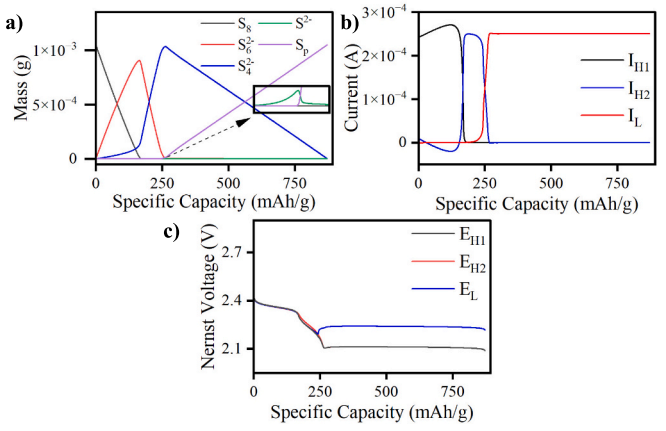


**Fig. 8.** Predicted $Li_2S$-Co@KB battery variables during the discharge process at a current rate of 0.2C, (a) Mass of sulfur species. (b) Reaction currents. (c) Nernst potentials.

Conversely, the slight decrease in $k_s$ suggests improved control over polysulfide shuttling, contributing to better coulombic efficiency even at elevated reaction rates. Overall, the observed increase in $I^0_{H1}$, $I^0_{H2}$, and $I^0_L$ and $k_p$, coupled with a reduction in $k_s$, highlights the LSB capability to support high current rates through the enhancement of reaction and precipitation kinetics while effectively mitigating the shuttle effect. However, the decrease in $E^0_{H1}$, $E^0_{H2}$, and $E^0_L$ underscores the presence of polarization issues due to resistive losses. This indicates that further optimization of the electrolyte composition and electrode structure is necessary to achieve efficient and stable operation at high discharge current rates.

It should be noted that by calibrating the model to achieve the same experimental specific capacity, variations in accessible sulfur mass are introduced as fitting parameters, which gives the ability to reproduce capacity trends without explicitly capturing transport limitations. In this way, the methodology focuses on data fitting of all parameters in the new C-rate instead of a direct physical model of internal processes. There are some mechanistic models in the literature [21,26] that attempt to account for dynamic changes in porosity and active surface area during discharge. This helps to better capture the evolution of electrode morphology and its impact on capacity, particularly during the second discharge plateau. However, to maintain computational efficiency and avoid the introduction of additional state variables that may compromise numerical stability, we approximate these effects by adjusting the utilized sulfur mass. Future work may involve incorporating lumped transport resistance elements such as electrolyte ionic resistance and solid-state diffusion limitations, and morphology-related parameters. These changes would improve the model's ability to reproduce the voltage slope and duration of the second plateau and could also allow for a better representation of rate-dependent capacity loss at different current densities.

## 4. Conclusion

This study presents a three-step 0D model for predicting the characteristics of LSBs during discharge, demonstrating its effectiveness in capturing key features of the discharge voltage curve. The model employs the Nernst equation to calculate the equilibrium potentials of electrochemical reactions and a Butler-Volmer approximation to describe the current-overpotential relationship, linking overpotentials to the total cell potential. Additionally, the model tracks the temporal changes in sulfur species due to production, consumption, the shuttle effect, and precipitation, inherently reflecting the impact of these phenomena on battery behaviour. The 0D model proves to be a valuable tool for studying the evolution of species concentrations and understanding the interplay between reaction kinetics and precipitation parameters, all while maintaining relatively modest computational demands. The proposed optimization methodology effectively parametrizes the 0D model for the as-synthesized $Li_2S$-Co@KB cathode. By combining local refinement with targeted error weighting in a multistage Bayesian optimization framework, the approach addresses the limitations of PSO. This hybrid method ensures a well-targeted optimization process, achieving better convergence and improved model accuracy within shorter computational times. The model is particularly effective in accurately predicting the behaviour around the dip point in the voltage curve, a critical feature in LSBs associated with important electrochemical processes during discharge. Accurate prediction of the dip point voltage is essential for battery management systems, enhancing their ability to control and optimize battery performance. One valuable application of this model is in battery balancing, where the identification of variations in dip point behaviour can help detect imbalances among connected batteries. Overall, this work highlights the importance of advanced modelling techniques in accurately representing the real-world performance of LSBs, ensuring that critical regions of the voltage curve are well-represented. This enhances the predictive reliability and practical

applicability of the simulation model. The proposed model serves as a robust tool for describing the inner dynamics of LSBs, providing a strong foundation for developing diagnostic and predictive techniques. Such techniques can help materials scientists evaluate LSB cell performance across various applications and optimize new material candidates. Furthermore, the model can be readily extended to incorporate the voltage contributions of novel anodes paired with S-based cathodes or to assess the impact of different electrolytes, making it a versatile framework for advancing LSB technology.

## CRediT authorship contribution statement

**Hamid Mollania:** Writing – original draft, Visualization, Validation, Software, Methodology, Investigation, Formal analysis, Data curation, Conceptualization. **Majid Oloomi-Buygi:** Writing – review & editing, Supervision, Resources, Project administration, Methodology. **Andreu Cabot:** Writing – review & editing, Supervision, Resources, Project administration.

## Declaration of competing interest

The authors declare no conflict of interest.

## Data availability

Data will be made available on request.

## References


[1] H. Ye, M. Li, T. Liu, Y. Li, J. Lu, Activating $Li_2S$ as the lithium-containing cathode in lithium–sulfur batteries, ACS Energy Lett. 5 (2020) 2234–2245, https://doi.org/10.1021/acsenergylett.0c00936.

[2] J. Xiang, Y. Zhao, L. Wang, C. Zha, The presolvation strategy of $Li_2S$ cathodes for lithium–sulfur batteries: a review, J. Mater. Chem. A 10 (2022) 10326–10341, https://doi.org/10.1039/d2ta01008a.

[3] H. Mollania, C. Zhang, R. Du, X. Qi, J. Li, S. Horta, M. Ibañez, C. Keller, P. Chenevier, M. Oloomi-Buygi, Nanostructured $Li_2S$ cathodes for silicon–sulfur batteries, ACS Appl. Mater. Interfaces 15 (2023) 58462–58475, https://doi.org/10.1021/acsami.3c14072.

[4] J. Jiang, Q. Fan, S. Chou, Z. Guo, K. Konstantinov, H. Liu, J. Wang, $Li_2S$-based Li-ion sulfur batteries: Progress and prospects, Small 17 (2021) e1903934, https://doi.org/10.1002/smll.201903934.

[5] S. Li, D. Leng, W. Li, L. Qie, Z. Dong, Z. Cheng, Z. Fan, Recent progress in developing $Li_2S$ cathodes for Li–S batteries, Energ. Storage Mater. 27 (2020) 279–296, https://doi.org/10.1016/j.ensm.2020.02.010.

[6] M. Yu, S. Zhou, Z. Wang, W. Pei, X. Liu, C. Liu, C. Yan, X. Meng, S. Wang, J. Zhao, J. Qiu, A molecular-cage strategy enabling efficient chemisorption–electrocatalytic interface in nanostructured $Li_2S$ cathode for Li metal-free rechargeable cells with high energy, Adv. Funct. Mater. 29 (2019), https://doi.org/10.1002/adfm.201905986.

[7] C. Zhang, B. Fei, D. Yang, H. Zhan, J. Wang, J. Diao, J. Li, G. Henkelman, D. Cai, J. J. Biendicho, J.R. Morante, A. Cabot, Robust lithium–sulfur batteries enabled by highly conductive $WSe_2$-based superlattices with tunable interlayer space, Adv. Funct. Mater. 32 (24) (2022) 2201322, https://doi.org/10.1002/adfm.202201322.

[8] M. Li, D. Yang, J.J. Biendicho, X. Han, C. Zhang, K. Liu, J. Diao, J. Li, J. Wang, M. Heggen, R.E. Dunin-Borkowski, J. Wang, G. Henkelman, J.R. Morante, J. Arbiol, S.L. Chou, A. Cabot, Enhanced polysulfide conversion with highly conductive and electrocatalytic iodine-doped bismuth selenide nanosheets in lithium–sulfur batteries, Adv. Funct. Mater. 32 (26) (2022) 2200529, https://doi.org/10.1002/adfm.202200529.

[9] H. Yuan, X. Chen, G. Zhou, W. Zhang, J. Luo, H. Huang, Y. Gan, C. Liang, Y. Xia, J. Zhang, J. Wang, X. Tao, Efficient activation of $Li_2S$ by transition metal phosphides nanoparticles for highly stable lithium–sulfur batteries, ACS Energ. Lett. 2 (2017) 1711–1719, https://doi.org/10.1021/acsenergylett.7b00465.

[10] S.F. Ng, M.Y.L. Lau, W.J. Ong, Lithium–sulfur battery cathode design: tailoring metal-based nanostructures for robust polysulfide adsorption and catalytic conversion, Adv. Mater. 33 (2021) 2008654, https://doi.org/10.1002/adma.202008654.

[11] A. Eftekhari, D.-W. Kim, Cathode materials for lithium–sulfur batteries: a practical perspective, J. Mater. Chem. A 5 (2017) 17734–17776, https://doi.org/10.1039/C7TA00799J.

[12] X. Yang, X. Li, K. Adair, H. Zhang, X. Sun, Structural design of lithium–sulfur batteries: from fundamental research to practical application, Electrochem. Energy Rev. 1 (2018) 239–293, https://doi.org/10.1007/s41918-018-0010-3.

[13] A. Fotouhi, D.J. Auger, K. Propp, S. Longo, Lithium–sulfur battery state-of-charge observability analysis and estimation, IEEE Trans. Power Electron. 33 (2017) 5847–5859, https://doi.org/10.1109/TPEL.2017.2740223.

[14] D. Su, D. Zhou, C. Wang, G. Wang, Toward high performance lithium–sulfur batteries based on $Li_2S$ cathodes and beyond: status, challenges, and perspectives, Adv. Funct. Mater. 28 (2018), https://doi.org/10.1002/adfm.201800154.

[15] K. Yoo, M.-K. Song, E.J. Cairns, P. Dutta, Numerical and experimental investigation of performance characteristics of lithium/sulfur cells, Electrochim. Acta 213 (2016) 174–185, https://doi.org/10.1016/j.electacta.2016.07.110.

[16] É.A. Santos, R.C. Fernandes, R. Vicentini, J.P. Aguiar, L.M. Da Silva, H. Zanin, On the electrochemical properties of lithium-sulfur batteries, J. Energy Storage 71 (2023) 108203, https://doi.org/10.1016/j.est.2023.108203.

[17] H. Mollania, M. Oloomi-Buygi, Low-cost $Li_2S$-based cathode for lithium sulfur battery, J. Ultrafine Grained Nanostruct. Mater. 57 (2024) 68–74, https://doi.org/10.22059/jufgnsm.2024.01.08.

[18] V. Sedlakova, J. Sikula, P. Sedlak, O. Cech, L. Urrutia, A simple analytical model of capacity fading for lithium–sulfur cells, IEEE Trans. Power Electron. 34 (2018) 5779–5786, https://doi.org/10.1109/TPEL.2018.2870250.

[19] K. Propp, D.J. Auger, A. Fotouhi, S. Longo, V. Knap, Kalman-variant estimators for state of charge in lithium-sulfur batteries, J. Power Sources 343 (2017) 254–267, https://doi.org/10.1016/j.jpowsour.2016.12.087.

[20] J.P. Rivera-Barrera, N. Muñoz-Galeano, H.O. Sarmiento-Maldonado, SoC estimation for lithium-ion batteries: review and future challenges, Electronics 6 (2017) 102, https://doi.org/10.3390/electronics6040102.

[21] Z. Huang, L.D. Couto, C. Dangwal, S. Xiao, W. Lv, D. Zhang, S.J. Moura, On electrochemical model-based state estimation for lithium–sulfur batteries, IEEE Trans. Control Syst. Technol. 32 (3) (2024) 849–861, https://doi.org/10.1109/TCST.2023.3337589.

[22] R. Zhang, B. Xia, B. Li, L. Cao, Y. Lai, W. Zheng, H. Wang, W. Wang, State of the art of lithium-ion battery SOC estimation for electrical vehicles, Energies 11 (2018) 1820, https://doi.org/10.3390/en11071820.

[23] G. Goujard, C. Dangwal, P. Gill, D. Kato, S.J. Moura, Modeling and state estimation for lithium sulfur batteries as a piecewise affine system, 2023 62nd IEEE Confe. Decis. Contr. (CDC) (2023) 184–190, https://doi.org/10.1109/CDC49753.2023.10383616.

[24] Z. Huang, D. Zhang, L.D. Couto, Q.-H. Yang, S.J. Moura, State estimation for a zero-dimensional electrochemical model of lithium-sulfur batteries, in: 2021 American Control Conference (ACC), 2021, pp. 3114–3119, https://doi.org/10.23919/ACC50511.2021.9483225.

[25] S.J. Moura, F.B. Argomedo, R. Klein, A. Mirtabatabaei, M. Krstic, Battery state estimation for a single particle model with electrolyte dynamics, IEEE Trans. Control Syst. Technol. 25 (2016) 453–468, https://doi.org/10.1109/TCST.2016.2571663.

[26] C. Xu, T. Cleary, G. Li, D. Wang, H. Fathy, Parameter identification and sensitivity analysis for zero-dimensional physics-based lithium-sulfur battery models, ASME Lett. Dyn. Syst. Contr. 1 (2021) 041001, https://doi.org/10.1115/1.4050125.

[27] Y.V. Mikhaylik, J.R. Akridge, Polysulfide shuttle study in the Li/S battery system, J. Electrochem. Soc. 151 (2004) A1969, https://doi.org/10.1149/1.1806394.

[28] M. Marinescu, T. Zhang, G.J. Offer, A zero dimensional model of lithium–sulfur batteries during charge and discharge, Phys. Chem. Chem. Phys. 18 (2016) 584–593, https://doi.org/10.1039/C5CP05755H.

[29] J. Newman, N.P. Balsara, Electrochemical systems, John Wiley & Sons, 2021.

[30] R. Melnik, A. Roberts, K. Thomas, Phase transitions in shape memory alloys with hyperbolic heat conduction and differential-algebraic models, Comput. Mech. 29 (2002) 16–26, https://doi.org/10.1007/s00466-002-0311-5.

[31] Q. Cheng, W. Xu, S. Qin, S. Das, T. Jin, A. Li, A.C. Li, B. Qie, P. Yao, H. Zhai, Full dissolution of the whole lithium sulfide family ($Li_2S_8$ to $Li_2S$) in a safe eutectic solvent for rechargeable lithium–sulfur batteries, Angew. Chem. 131 (2019) 5613–5617, https://doi.org/10.1002/anie.201812611.

[32] H.A. Adeoye, M. Dent, J.F. Watts, S. Tennison, C. Lekakou, Solubility and dissolution kinetics of sulfur and sulfides in electrolyte solvents for lithium–sulfur and sodium–sulfur batteries, J. Chem. Phys. 158 (2023), https://doi.org/10.1063/5.0132068.

[33] D. Wang, D. Tan, L. Liu, Particle swarm optimization algorithm: an overview, Soft. Comput. 22 (2018) 387–408, https://doi.org/10.1007/s00500-016-2474-6.

[34] B. Shahriari, K. Swersky, Z. Wang, R.P. Adams, N. De Freitas, Taking the human out of the loop: a review of Bayesian optimization, Proc. IEEE 104 (2015) 148–175, https://doi.org/10.1109/JPROC.2015.2494218.

[35] P.I. Frazier, A tutorial on Bayesian optimization, in: arXiv Preprint arXiv: 1807.02811, 2018, https://doi.org/10.48550/arXiv.1807.02811.

[36] S. Takenaga, Y. Ozaki, M. Onishi, Practical initialization of the Nelder–Mead method for computationally expensive optimization problems, Optim. Lett. 17 (2023) 283–297, https://doi.org/10.1007/s11590-022-01953-y.

[37] J.C. Lagarias, J.A. Reeds, M.H. Wright, P.E. Wright, Convergence properties of the Nelder-Mead simplex method in low dimensions, SIAM J. Optim. 9 (1998) 112–147, https://doi.org/10.1137/S1052623496303470.

[38] Z. Nozarijouybari, C. Fang, M. Doosthosseini, C. Xu, H.K. Fathy, An algorithm for dip point detection in lithium–sulfur battery cells, J. Energy Storage 55 (2022) 105665, https://doi.org/10.1016/j.est.2022.105665.

[39] T. Zhang, M. Marinescu, L. O'Neill, M. Wild, G. Offer, Modeling the voltage loss mechanisms in lithium–sulfur cells: the importance of electrolyte resistance and precipitation kinetics, Phys. Chem. Chem. Phys. 17 (2015) 22581–22586, https://doi.org/10.1039/C5CP03566J.